(Preprint) AAS 15-815

ORBITAL MANEUVERING SYSTEM DESIGN AND PERFORMANCE FOR THE MAGNETOSPHERIC MULTISCALE FORMATION

Steven Z. Queen[*], Dean J. Chai[*], and Sam Placanica[*]

The Magnetospheric Multiscale (MMS) mission consists of four identically instrumented, spin-stabilized observatories elliptically orbiting the Earth in a tetrahedron formation. A requirement for the operational success of the mission is the ability for the on-board systems to deliver precise maneuver adjustments. A six degree-of-freedom (6-DOF), closed-loop control system was developed that tracks a time-varying, inertial velocity-target with less than 1% error down to a five millimeter-per-second lower-threshold (3σ). This level of performance is achieved in-part through integrated and dynamically-compensated accelerometer feedback with micro-gravity resolution. System performance is bounded through an extensive Monte Carlo simulation campaign that exercises the multi-body dynamics and non-linear sensitivities, and supported by some initial flight-results.

INTRODUCTION

The Magnetospheric Multiscale (MMS) mission, launched on March 13, 2015, is the fourth mission of NASA's Solar Terrestrial Probe program. The MMS mission consists of four identically instrumented observatories that function as a constellation to provide the first definitive study of magnetic reconnection in space.

Since it is frequently desirable to isolate electric and magnetic field sensors from stray effects caused by the spacecraft's core-body, the suite of instruments on MMS includes six radial and two axial instrument-booms with deployed lengths ranging from 5–60 meters (see Figure 1). The observatory is spin-stabilized about its positive z-axis with a nominal rate slightly above 3 rev/min (RPM). The spin is also used to maintain tension in the four radial wire-booms.

Each observatory's Attitude Control System (ACS) consists of digital sun sensors, star cameras, accelerometers, and mono-propellant hydrazine thrusters—responsible for orbital adjustments, attitude control, and spin adjustments. The sections that follow describe performance requirements, the hardware and algorithms used for 6-DOF estimation, and then similarly for 6-DOF control. The paper concludes with maneuver performance based on both simulated and on-orbit telemetry.

Performance Requirements

Once in science mission orbits, the four 0.12-km diameter observatories plan to form a tetrahedron with as little as 4-km of separation between spacecraft. The need to maintain a sufficiently

[*] Aerospace Engineer, Attitude Control Systems Engineering Branch, NASA/GSFC, Greenbelt, MD.

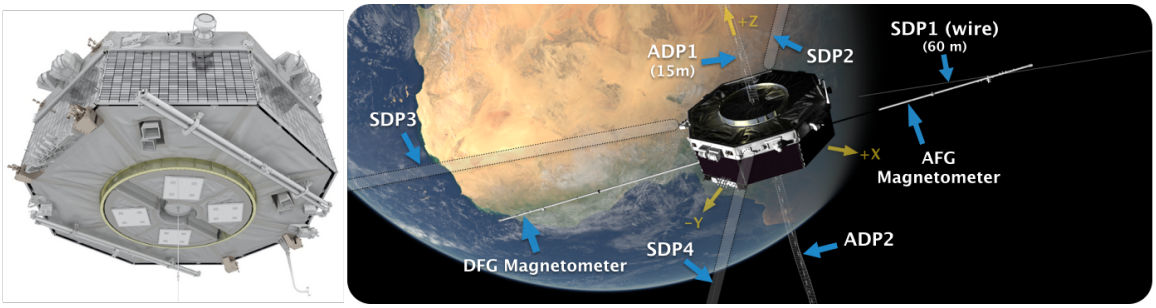

Figure 1. MMS Observatory (Stowed / Fully-Deployed)

accurate spatial and temporal formation must be balanced against the logistical constraints of executing overly-frequent maneuvers on a fleet of spacecraft. These two considerations make for an extremely challenging orbit design problem.[1,2]

With a stated operational goal of maneuvering the fleet no more often than once every two weeks (on average), MMS flight dynamics specialists derived the formation maintenance maneuver execution requirements shown to the right.

Maneuver Size	**Error Allocation** (3σ)	
(m/sec)	Magnitude	Direction*
0 – 0.05	5 mm/sec	$40° \rightarrow 5°$
0.05 – 0.10	1%	$5° \rightarrow 1.5°$
0.10 <	1%	$1.5°$

* ($\rightarrow$ indicates linear decrease vs. size)

ATTITUDE, RATE, AND ACCELERATION

Star Sensor

The μASC Star Sensor System (STS), provided by the Technical University of Denmark, consists of internally redundant electronics housed within a single enclosure that interfaces with four Charge-Coupled Device camera head units. The STS provides time-stamped attitude quaternion data packets at a 4 Hz telemetry rate. It has a 3σ full performance transverse and boresight axis accuracy of 60 arcsec and 200 arcsec, respectively. The STS has a spin rate capability of up to 4 RPM. Figure 2 shows a 752×580 pixel image taken April 27, 2015 by Observatory 3 (MMS-3) using STS camera head unit B.

Figure 2. DTU μASC Image (OBS 3, CHU B)

Multiplicative Extended Kalman Filter (MEKF)

Attitude and angular rate of the spacecraft with respect to the ECI J2000 inertially fixed reference frame are determined on-board by processing the four quaternion solutions produced by each star sensor camera-head unit (CHU) at 4 Hz. The CHU measurements are transformed into the common spacecraft body-fixed frame and then combined in a Multiplicative Extended Kalman Filter

(MEKF). Due to limitations in the processing-power of the flight computer (Motorola RH-CF5208 Coldfire), neither the sun sensor nor the acceleration measurements are included in the filter's computations. Also, due to an early programmatic design-trade, MMS does not include gyroscopes in its complement of sensor. As a result, the MEKF does not use the standard gyro-replacement model and instead follows the method of Thienel, Markley and Harman.[3] A brief overview of the MMS on-board algorithm follows. The presentation assumes familiarity with the application of Kalman filters for spacecraft attitude estimation. As a result, only the elements particular to our system model will be discussed. A more complete explanation of the MEKF mechanics (covariance/gains/update equations, etc.) can be found in the references.[4,5]

States The MMS filter uses a seven-component vector consisting of the body's attitude quaternion $\mathbf{q}$ and the angular rate $\boldsymbol{\omega}$ for its full-state $\mathbf{X}(\mathbf{q}, \boldsymbol{\omega})$, and a reduced six-component based on the *Gibbs vector* $\boldsymbol{\alpha}$ attitude representation for its error-state $\boldsymbol{x}(\boldsymbol{\alpha}, \boldsymbol{\delta\omega})$. The relationship between the error-quaternion $\boldsymbol{\delta q}$ (defined as the difference in attitude between the true attitude $\mathbf{q}$ at the time of measurement and the propagated estimate $\hat{\mathbf{q}}^-$) and the Gibbs vector is, to 1st-order,

$$\boldsymbol{\delta q} \equiv \mathbf{q} \otimes (\hat{\mathbf{q}}^-)^{-1} \approx \begin{bmatrix} \frac{\boldsymbol{\alpha}}{2} \\ 1 \end{bmatrix} \tag{1}$$

where the operator $\otimes$ denotes the quaternion product.[5]

Measurements for Update The star sensor measurement equation is simply the measured quaternion of the individual camera-heads transformed to the base-body frame,

$$\mathbf{y} = \mathbf{h}(\mathbf{q}, t) + \text{noise} = \mathbf{q}_{\mathsf{chu}} \tag{2}$$

Since the MEKF error states are "reset" after an update and completely absorbed in the full-state estimate (i.e. $\hat{\boldsymbol{\alpha}}^+ \equiv \mathbf{0}$), the measurement residuals $\boldsymbol{\rho}$ is equal to the quaternion product between the *a priori* attitude quaternion estimate $\hat{\mathbf{q}}^-$ and the current measurement,

$$\boldsymbol{\rho} = \mathbf{y} - \mathbf{h}\left(\hat{\mathbf{q}}\right) - \mathbf{H}_\alpha \hat{\boldsymbol{\alpha}}^+ \tag{3}$$

$$= \boldsymbol{\alpha}_{\mathsf{chu}} = 2 \cdot \boldsymbol{\delta q}_{(1:3)} \cdot \text{sign}\left(\delta q_4\right) \tag{4}$$

where q_4 is the quaternion scalar, and $\mathbf{H}_\alpha$ is a component of the linearized measurement sensitivity matrix,

$$\mathbf{H} = \begin{bmatrix} \frac{\partial \mathbf{h}}{\partial \boldsymbol{\alpha}} & \frac{\partial \mathbf{h}}{\partial \boldsymbol{\omega}} \end{bmatrix}_{\hat{\mathbf{X}}} = \begin{bmatrix} \mathbf{H}_\alpha & \mathbf{H}_\omega \end{bmatrix} = \begin{bmatrix} \mathbb{I} & \mathbf{0} \end{bmatrix} \tag{5}$$

and $\mathbb{I}$ is a 3×3 identity matrix.

Model The full non-linear state dynamics,

$$\dot{\mathbf{X}} = \mathbf{f}\left(\mathbf{X}, \hat{\mathbf{u}}, t\right) + \mathbf{w}(t) = \begin{Bmatrix} \mathbf{f}_\alpha \\ \mathbf{f}_\omega \end{Bmatrix} + \mathbf{w}(t) \tag{6}$$

$$= \begin{Bmatrix} \dot{\mathbf{q}} = & \frac{1}{2} \begin{bmatrix} -\boldsymbol{\omega}^\times & \boldsymbol{\omega} \\ \boldsymbol{\omega}^\mathsf{T} & 1 \end{bmatrix} \mathbf{q} \\ \dot{\boldsymbol{\omega}} = & \mathbf{I}^{-1}\left[\boldsymbol{\tau}(\mathbf{u}) - \boldsymbol{\omega}^\times \mathbf{I}\boldsymbol{\omega}\right] \end{Bmatrix} + \mathbf{w}(t) \tag{7}$$

$$\approx \mathbf{f}\left(\hat{\mathbf{X}}, \mathbf{u}, t\right) + \left.\frac{\partial \mathbf{f}}{\partial \mathbf{X}}\right|_{\hat{\mathbf{X}}} \cdot \mathbf{x} + \left.\frac{\partial \mathbf{f}}{\partial \mathbf{u}}\right|_{\mathbf{u}} \cdot \mathbf{u} + \mathbf{w}(t) \tag{8}$$

are the quaternion kinematics and *Euler's rotational equation*, driven by the control-input torque $\boldsymbol{\tau}(\mathbf{u})$ and white noise $\mathbf{w}$. The superscript expression $[]^{\mathsf{T}}$ is the matrix transpose, and $[]^{\times}$ denotes a skew-symmetric 3×3 matrix formed from the base vector. For example,

$$\boldsymbol{\omega}^{\times} = \begin{bmatrix} \omega_x \\ \omega_y \\ \omega_z \end{bmatrix}^{\times} = \begin{bmatrix} 0 & -\omega_z & \omega_y \\ \omega_z & 0 & \omega_x \\ -\omega_y & \omega_x & 0 \end{bmatrix} \tag{9}$$

Also, note that the presence of the body's second mass-moment of inertia $\mathbf{I}$ in Eq. (7) requires accurate knowledge of the inertia mass properties for rate estimation—something that is typically avoided via direct substitution of angular rate measurements from a high-quality gyroscope.

The associated error state dynamics are

$$\dot{\mathbf{x}} = \mathbf{F}\mathbf{x} + \mathbf{G}\mathbf{u} + \mathbf{w} \tag{10}$$

$$\begin{bmatrix} \dot{\boldsymbol{\alpha}} \\ \dot{\boldsymbol{\delta\omega}} \end{bmatrix} = \begin{bmatrix} \dfrac{\partial \boldsymbol{f}_{\alpha}}{\partial \boldsymbol{\alpha}} & \dfrac{\partial \boldsymbol{f}_{\alpha}}{\partial \boldsymbol{\omega}} \\ \dfrac{\partial \boldsymbol{f}_{\omega}}{\partial \boldsymbol{\alpha}} & \dfrac{\partial \boldsymbol{f}_{\omega}}{\partial \boldsymbol{\omega}} \end{bmatrix}_{\hat{\mathbf{x}}} \begin{bmatrix} \boldsymbol{\alpha} \\ \boldsymbol{\delta\omega} \end{bmatrix} + \begin{bmatrix} \dfrac{\partial \boldsymbol{f}_{\boldsymbol{\alpha}}}{\partial \boldsymbol{u}} \\ \dfrac{\partial \boldsymbol{f}_{\boldsymbol{\omega}}}{\partial \boldsymbol{u}} \end{bmatrix} \mathbf{u} + \mathbf{w} \tag{11}$$

$$= \begin{bmatrix} -\hat{\boldsymbol{\omega}}^{\times} & \mathbb{I} \\ \mathbf{0} & \mathbf{I}^{-1}\left[(\mathbf{I}\hat{\boldsymbol{\omega}})^{\times} - \hat{\boldsymbol{\omega}}^{\times}\mathbf{I}\right] \end{bmatrix} \begin{bmatrix} \boldsymbol{\alpha} \\ \boldsymbol{\delta\omega} \end{bmatrix} + \begin{bmatrix} \mathbf{0} \\ \mathbf{I}^{-1}\boldsymbol{\tau} \end{bmatrix} \mathbf{u} + \mathbf{w} \tag{12}$$

Full State Update In an MEKF, the full-state estimate update for the angular rate is made additively ($\hat{\boldsymbol{\omega}}^{+} = \boldsymbol{\delta\omega} + \hat{\boldsymbol{\omega}}^{-}$), and multiplicatively for the attitude quaternion ($\hat{\boldsymbol{q}}^{+} = \boldsymbol{\delta q} \otimes \hat{\boldsymbol{q}}^{-}$).[4]

Performance Telemetered flight data shows unbiased measurement residuals of roughly 50-arcsec (3σ) for transverse attitude errors ($\Delta\theta_{x,y}$) and 500-arsec (3σ) about the spin-axis. Those numbers are consistent with attitude estimation errors of 40 and 110-arcsec (3σ) respectively (versus simulated truth). Similarly, the associated angular rate estimation errors are 0.01 and 0.03-deg/sec (3σ) during non-thrusting periods—with errors peaking 3–6 times greater while thrusting. A more detailed examination of the MEKF's performance is planned for a future publication.

Acceleration Measurement System (AMS)

The Acceleration Measurement System (AMS), which was manufactured by ZIN Technologies of Cleveland, Ohio, provides three-axis acceleration measurements during orbit-adjustments and integrates these samples in order to help determine the net velocity change (Δv) imparted by these maneuvers. The AMS incorporates internally redundant electronics within a single enclosure with each side interfacing with its own set of three single-axis orthogonally mounted Honeywell QA3000 accelerometer sensors. The AMS electronics include high-rate (100 kHz) analog-to-digital signal conversion. An embedded processor down-samples and filters the acceleration data. The AMS has a dynamic range of greater than $\pm$25,000 μg, a resolution of less than 1 μg, a short-term, 1σ bias stability over a twelve hour period of better than 1 μg, and an effective bandwidth of 250 Hz.

Accelerometer Dynamical Model

An accelerometer behaves dynamically as if it were a small proof-mass attached to a central-body by relatively stiff tri-axial springs. The device then generates a measurement signal proportional to

a (small) displacement $\boldsymbol{\xi}$ relative to its non-accelerating (rest) state. This conceptual model is sufficient for most applications regardless of the actual device's internal construction (e.g. cantilevered beam, electro-magnetic re-balance loop, etc.).

Given the accelerometer's proof-mass position $\mathbf{R}_p$ with respect to an inertially-fixed origin is equivalent to the location of a body-fixed origin's inertial position ($\mathbf{R}_o$) summed with a local vector ($\mathbf{r}_d$) that places the device's in body-fixed coordinates, plus the proof-mass' deflection from its rest-state. This relationship is expressed as the equation

$$\mathbf{R}_p = \mathbf{R}_o + \underset{i\leftarrow b}{\mathcal{A}} \underbrace{(\mathbf{r}_d + \boldsymbol{\xi})}_{\mathbf{r}_p} \tag{13}$$

where the symbol $\mathcal{A}$ is used generally in this paper to denote an attitude direction-cosine matrix, and in this specific instance is the transformation from the body-fixed to inertial frame. Twice differentiating Eq. (13) with respect to time produces the kinematic acceleration of the device-mass m_p with respect to the inertial frame as

$$\dot{\mathbf{V}}_p = \frac{d^2}{dt}\mathbf{R}_p = \dot{\mathbf{V}}_o + \underset{i\leftarrow b}{\mathcal{A}} \left(\dot{\boldsymbol{\omega}}^{\times}\mathbf{r}_p + \boldsymbol{\omega}^{\times}\boldsymbol{\omega}^{\times}\mathbf{r}_p + 2\cdot\boldsymbol{\omega}^{\times}\dot{\mathbf{r}}_p + \ddot{\mathbf{r}}_p\right) \tag{14}$$

where $\boldsymbol{\omega}$ is the angular velocity of the body-fixed frame with respect to the inertial frame, expressed in body coordinates. Assuming the tiny proof-mass deflections are much smaller than the vector locating the device in the body-frame, then $\mathbf{r}_p \approx \mathbf{r}_d$. If we also neglect structural flexure of the base-body, then rigidity implies $\dot{\mathbf{r}}_d = \ddot{\mathbf{r}}_d = 0$, and the kinematic expression of Eq. (14) reduces even further. Substituting for the acceleration at the sensor-head into *Newton's second law of motion*, equates the total proof-mass acceleration to the sum of the external forces acting on it as follows

$$\sum \mathbf{F}_p = m_p\dot{\mathbf{V}}_p \tag{15}$$

$$m_p\cdot\mathbf{a}_{\mathsf{grav}} - \underset{i\leftarrow b}{\mathcal{A}}\left(c_d\,\dot{\boldsymbol{\xi}} + k_d\,\boldsymbol{\xi}\right) = m_p\left[\dot{\mathbf{V}}_o + \underset{i\leftarrow b}{\mathcal{A}}\left(\dot{\boldsymbol{\omega}}^{\times}\mathbf{r}_d + \boldsymbol{\omega}^{\times}\boldsymbol{\omega}^{\times}\mathbf{r}_d + \boldsymbol{\omega}^{\times}\dot{\boldsymbol{\xi}}\right)\right] \tag{16}$$

where $\mathbf{a}_{\mathsf{grav}}$ is the acceleration due to a gravitational field. Eq. (16) also moved $\ddot{\mathbf{r}}_p = \ddot{\boldsymbol{\xi}}$ to the left-hand side of the equality, and uses *Newton's third law* to replace the proof-mass acceleration $\ddot{\boldsymbol{\xi}}$ with the tri-axial spring-force (c_d is the damping coefficient of the spring, and k_d its stiffness). If the dynamics-of-interest are far enough below the bandwidth of the sensor ($\dot{\mathbf{V}}_o, \dot{\boldsymbol{\omega}} \ll \frac{k_d}{m_p}$), the accelerometer's internal response will have damped out ($\dot{\boldsymbol{\xi}} \rightarrow \mathbf{0}$), and the device will produce a steady-state output

$$\mathbf{a}_d \equiv -\tfrac{k_d}{m_p}\boldsymbol{\xi} = \underset{b\leftarrow i}{\mathcal{A}}\left(\dot{\mathbf{V}}_o - \mathbf{a}_{\mathsf{grav}}\right) + \dot{\boldsymbol{\omega}}^{\times}\mathbf{r}_d + \boldsymbol{\omega}^{\times}\boldsymbol{\omega}^{\times}\mathbf{r}_d \tag{17}$$

Note that the only external force the device's proof-mass experiences is gravity, because it is a field-effect. All other mechanical disturbances to the system must be transmitted through the base-body via the tri-axial spring. Prior to launch, resting on a clean-room floor, the accelerometer "sees" gravity on its output because the base-structure is at rest ($\dot{\mathbf{V}}_o \approx 0$, unless of course there is an earthquake or heavy-footed technician nearby). In orbit, the expression for the base-body's acceleration with respect to inertial can be obtained by differentiating the linear momentum $\mathbf{P}$ of

the base-body with respect to the inertial frame,

$$\dot{\mathbf{P}} = m\dot{\mathbf{V}}_c + \dot{m}\left(\mathbf{V}_c - \mathbf{V}_{\dot{m}}\right) = m\frac{d^2}{dt}\left(\mathbf{R}_o + \underset{i\leftarrow b}{\mathcal{A}}\mathbf{r}_c\right) + \dot{m}\,\boldsymbol{\delta v}_{\dot{m}} \tag{18}$$

$$= m\left[\dot{\mathbf{V}}_o + \underset{i\leftarrow b}{\mathcal{A}}\left(\ddot{\mathbf{r}}_c + \dot{\boldsymbol{\omega}}^{\times}\mathbf{r}_c + 2\boldsymbol{\omega}^{\times}\dot{\mathbf{r}}_c + \boldsymbol{\omega}^{\times}\boldsymbol{\omega}^{\times}\mathbf{r}_c\right)\right] \tag{19}$$

where $\mathbf{r}_c$ is the position of the base-body's center-of-mass (CM) expressed in the body-fixed frame, m is the spacecraft mass, and $\boldsymbol{\delta v}_{\dot{m}}$ is a relative exhaust velocity of any expelled mass (e.g. thrusters). Even though a rigid-base was assumed in the derivation of the proof-mass motion, choosing not to nullify the derivatives of the CM at this point provides a placeholder for multi-body effects such as fuel-slosh and appendage motion, so they remain intact for now. Applying *Newton's second law* and identifying the mass-expulsion as the body-fixed thruster-force ($\mathbf{f}_t$), Eq. (19) now takes the form

$$\dot{\mathbf{V}}_o = \frac{1}{m}\sum \mathbf{F}_b - \underset{i\leftarrow b}{\mathcal{A}}\left(\ddot{\mathbf{r}}_c + \dot{\boldsymbol{\omega}}^{\times}\mathbf{r}_c + 2\boldsymbol{\omega}^{\times}\dot{\mathbf{r}}_c + \boldsymbol{\omega}^{\times}\boldsymbol{\omega}^{\times}\mathbf{r}_c\right) \tag{20}$$

$$= \mathbf{a}_{\mathsf{grav}} + \underset{i\leftarrow b}{\mathcal{A}}\left(\frac{k_d}{m}\boldsymbol{\xi} + \frac{\mathbf{f}_{\mathsf{t}}}{m} - \ddot{\mathbf{r}}_c - \dot{\boldsymbol{\omega}}^{\times}\mathbf{r}_c - 2\cdot\boldsymbol{\omega}^{\times}\dot{\mathbf{r}}_c - \boldsymbol{\omega}^{\times}\boldsymbol{\omega}^{\times}\mathbf{r}_c\right) \tag{21}$$

Assuming that the accelerometer proof-mass is much smaller than that of the base-body ($m_d \ll m$), the spring reaction-force $\frac{k_d}{m}\boldsymbol{\xi}$ can be ignored without inducing significant error. Finally, combining Eq. (21) with Eq. (17) yields a complete expression for an accelerometer truth-model

$$\mathbf{a}_d = \frac{\mathbf{f}_{\mathsf{t}}}{m} + \dot{\boldsymbol{\omega}}^{\times}\underbrace{\left(\mathbf{r}_d - \mathbf{r}_c\right)}_{\mathbf{r}_{cd}} + \boldsymbol{\omega}^{\times}\boldsymbol{\omega}^{\times}\left(\mathbf{r}_d - \mathbf{r}_c\right) - \underbrace{\left(2\cdot\boldsymbol{\omega}^{\times}\dot{\mathbf{r}}_c + \ddot{\mathbf{r}}_c\right)}_{\text{multi-body effects}} \tag{22}$$

It its interesting to note the cancellation of the gravitational acceleration terms between the two equations. In truth, this only holds if the gravitational field is completely uniform. However, with the semi-major axis of the MMS orbit varying from 1.2–12 Earth radii, the so-called *gravity-gradient effect* (defined as the difference in the gravitational field across the spacecraft) is negligible. Specifically, using those inverse-squared distances with a CM-to-sensor displacement ($\mathbf{r}_{cd}$) of only one meter produces a maximum effect of $0.18\,\mu$g at perigee and $2\times10^{-4}\,\mu$g at apogee—sufficiently below the threshold of the MMS accelerometer.

Measurement Equation

A discrete-sample at time t_k of the acceleration from the n^{th} sensor-head, a_n, is modeled as

$$a_n(t_k) = (1+\delta\kappa_n)\cdot\hat{\mathbf{u}}_n^{\mathsf{T}}\mathbf{a}_d + b_n + \eta_n \tag{23}$$

where $\delta\kappa_b$ is a scale factor error, $\hat{\mathbf{u}}$ is a unit vector along the true sensing axis of the n^{th} sensor head, b_n is an intrinsic electro-mechanical bias, and η_n is sensor noise (possibly non-white). All of the introduced quantities $(\delta\kappa, \hat{\mathbf{u}}, b, \eta)$ are both time-varying and functions of temperature. A vector quantity for the sampled acceleration ($\mathbf{a}_k$) in the body-fixed frame can be reconstructed from the n (≥ 3) measurements using the pseudo-inverse of a user-supplied orthogonality matrix $\mathcal{O}$, which ideally cancels the true alignment matrix $\mathcal{U} = \begin{bmatrix}\mathbf{u}_1 & \mathbf{u}_2 & \dots & \mathbf{u}_n\end{bmatrix}^{\mathsf{T}}$ and scale-factor errors in a

manner for which

$$\mathbf{a}_k = \begin{bmatrix} a_x \\ a_y \\ a_z \end{bmatrix}_{t_k} = \underbrace{\left(\mathcal{O}^{\mathsf{T}}\mathcal{O}\right)^{-1}\mathcal{O}^{\mathsf{T}}}_{\mathsf{pseudo-inverse}} \left\{ \begin{bmatrix} (1+\delta\kappa_1)\,\hat{\mathbf{u}}_1^{\mathsf{T}} \\ (1+\delta\kappa_2)\,\hat{\mathbf{u}}_2^{\mathsf{T}} \\ \vdots \\ (1+\delta\kappa_n)\,\hat{\mathbf{u}}_n^{\mathsf{T}} \end{bmatrix} \mathbf{a}_d + \begin{bmatrix} b_1 \\ b_2 \\ \vdots \\ b_n \end{bmatrix} + \begin{bmatrix} \eta_1 \\ \eta_2 \\ \vdots \\ \eta_n \end{bmatrix} \right\} \tag{24}$$

holds true. In the case of MMS, the number of sensor heads is three ($n = 3$) and—through extensive ground calibration and on-orbit temperature control—they are believed to be nearly orthogonal. For the sake of simplicity in the explication that follows, it is assumed the scale factor, non-orthogonality, and alignment errors are essentially zero (although the full effects of the errors are bounded and included in the subsequent Monte Carlo analysis). With the stated assumptions, $\mathcal{U}$ and $\mathcal{O}$ are both the identity matrix $\mathbb{I}$, and Eq. (24) reduces to

$$\mathbf{a}_k = \mathbf{a}_d + \mathbf{b} + \boldsymbol{\eta} \tag{25}$$

VELOCITY ESTIMATION

The quantity of interest from a formation-maintenance perspective is not the acceleration *per se*, but the change in velocity of the spacecraft's center-of-mass due to thrusting. Analogous to a rate-integrating-gyro for attitude dynamics, the AMS's primary function for the mission is to act as an acceleration-integrating-accelerometer during orbital-adjustments. Combining Eq. (25) with Eq. (22), transforming to the inertial frame, and integrating over the time-interval (t_1, t_2) produces the following relationship

$$\begin{aligned} \int_{t_1}^{t_2} \underset{i\leftarrow b}{\mathcal{A}}\, \mathbf{a}_k \, d\tau \;\; = \;\; & \int_{t_1}^{t_2} \underset{i\leftarrow b}{\mathcal{A}}\, \frac{\mathbf{f}_t}{m}\, d\tau + \int_{t_1}^{t_2} \underset{i\leftarrow b}{\mathcal{A}}\, \left(\dot{\boldsymbol{\omega}}^{\times}\mathbf{r}_{cd} + \boldsymbol{\omega}^{\times}\boldsymbol{\omega}^{\times}\mathbf{r}_{cd}\right)\, d\tau \\ & - \int_{t_1}^{t_2} \underset{i\leftarrow b}{\mathcal{A}}\, \left(2\cdot\boldsymbol{\omega}^{\times}\dot{\mathbf{r}}_c + \ddot{\mathbf{r}}_c\right)\, d\tau + \int_{t_1}^{t_2} \underset{i\leftarrow b}{\mathcal{A}}\, \mathbf{b}\, d\tau + \int_{t_1}^{t_2} \underset{i\leftarrow b}{\mathcal{A}}\, \boldsymbol{\eta}\, d\tau \end{aligned} \tag{26}$$

Evaluating the definite integral, and denoting the integrated thrust as the perturbed velocity of the spacecraft's center-of-mass $\boldsymbol{\delta v}_c(t)$ the relationship takes the form

$$\begin{aligned} \int_{t_1}^{t_2} \underset{i\leftarrow b}{\mathcal{A}}\, \mathbf{a}_k \, d\tau = \boldsymbol{\delta v}_c(t_2) - \boldsymbol{\delta v}_c(t_1) + \underset{i\leftarrow b_2}{\mathcal{A}}\, [\boldsymbol{\omega}(t_2)]^{\times}\mathbf{r}_{cd}(t_2) - \underset{i\leftarrow b_1}{\mathcal{A}}\, [\boldsymbol{\omega}(t_1)]^{\times}\mathbf{r}_{cd}(t_1) \\ - \underset{i\leftarrow b_2}{\mathcal{A}}\, \dot{\mathbf{r}}_{\mathbf{c}}(t_2) + \underset{i\leftarrow b_1}{\mathcal{A}}\, \dot{\mathbf{r}}_{\mathbf{c}}(t_1) + \int_{t_1}^{t_2} \underset{i\leftarrow b}{\mathcal{A}}\, \mathbf{b}\, d\tau + \int_{t_1}^{t_2} \underset{i\leftarrow b}{\mathcal{A}}\, \boldsymbol{\eta}\, d\tau \end{aligned} \tag{27}$$

where the attitude matrix subscripts b_1 and b_2 refer to the body's orientation at times t_1 and t_2 respectively. Delaying the expansion of the definite integral limits to compress terms, we arrive at an important result. On the left-hand side of the following expression is the true quantity to be controlled, $\Delta\mathbf{v}_c$, and on the right an expression for it in terms of ideal integrated sensor measurements and some additional "error" sources that must be removed (estimated/compensated) in order to achieve precise maneuvering.

$$\underbrace{\Delta\mathbf{v}_c(t_1,t_2)}_{\mathsf{truth\ states}} = \underbrace{\int_{t_1}^{t_2} \underset{i\leftarrow b}{\mathcal{A}}\, \mathbf{a}_k \, d\tau}_{\mathsf{measurement}} + \underbrace{\left\{ \underset{i\leftarrow b}{\mathcal{A}}\, \boldsymbol{\omega}^{\times}\mathbf{r}_{cd} \right\}}_{\mathsf{centripetal}} - \underbrace{\left\{ \underset{i\leftarrow b}{\mathcal{A}}\, \dot{\mathbf{r}}_c \right\}_{t_1}^{t_2}}_{\mathsf{multi\text{-}body}} - \underbrace{\int_{t_1}^{t_2} \underset{i\leftarrow b}{\mathcal{A}}\, \mathbf{b}\, d\tau}_{\mathsf{bias}} - \underbrace{\int_{t_1}^{t_2} \underset{i\leftarrow b}{\mathcal{A}}\, \boldsymbol{\eta}\, d\tau}_{\mathsf{noise}} \tag{28}$$

Methods for estimating the terms of the right-hand side of Eq. (28) will be detailed in the sections that follow.

Measurement Integral

The first term on the right-hand side of Eq. (28), the measurement integral, is obtained by sampling the analog accelerometer (e.g. QA 3000) at a sufficiently high rate to capture all the relevant dynamics of the maneuvering spacecraft. In the case of MMS, the AMS electronics samples well above 1 kHz, and then applies appropriate decimation, anti-aliasing and noise reduction filters to deliver a "clean" 1 kHz digital signal. The discrete AMS output has a bandwidth of 250 Hz, and less than ± 5 ppm of gain and/or $\pm 1^\circ$ of phase distortion in the pass-band. Since the MMS ACS operates on a 4 Hz control cycle, the measurement integral contains 250 subsamples that are combined to generate a single velocity-increment. Outside the AMS, in the ACS flight software, the subinterval sample is transformed into the inertial frame, and summed to produce the total maneuver velocity-change estimate for closed-loop control.

Frame Rotation Compensation Because the summation of the subsamples must occur in a uniform reference frame, each subsample is transformed forward in time to what is assumed will be the frame of the final ($k = 250$) sample. This transformation is based upon the current estimate of the spacecraft's expected attitude motion. The propagation assumes the base-body's angular rate estimate $\hat{\boldsymbol{\omega}}(t_1)$ is approximately constant over the full quarter-second sample interval. In the parlance of strap-down inertial navigation systems, this type of compensation to the velocity update is known as a *sculling* correction.[6,7] (For reference, the dual term applied to gyro measurements for attitude updates is referred to as a *coning* correction.)

Recalling the measurement integral term of Eq. (28), its discrete approximation is

$$\int_{t_1}^{t_2} \underset{i\leftarrow b}{\mathcal{A}}(\tau)\, \mathbf{a}_k \, d\tau \approx \underset{i\leftarrow 250}{\mathcal{A}} \sum_{k=1}^{250} \underset{250\leftarrow k}{\mathcal{A}}(\hat{\boldsymbol{\omega}}, k) \cdot \mathbf{a}_k \cdot (t_k - t_{k-1}) \tag{29}$$

where the attitude matrix update is obtained from an *Euler axis/angle* parametrization[5]

$$\underset{250\leftarrow k}{\mathcal{A}}(\hat{\mathbf{e}}, \Phi_k) = \mathbb{I} - \sin\Phi_k \hat{\boldsymbol{e}}^\times + (1 - \cos\Phi_k)\, \hat{\boldsymbol{e}}^\times \hat{\boldsymbol{e}}^\times \tag{30}$$

where the Euler axis $\hat{\mathbf{e}} = \hat{\boldsymbol{\omega}}/\|\hat{\boldsymbol{\omega}}\|$ is a unit vector in the direction of the angular rate $\boldsymbol{\omega}$ expressed in body-fixed coordinates, and the Euler angle Φ is a function of the time-difference between the current (k^{th}) and final (250^{th}) sample,

$$\Phi_k = \|\hat{\boldsymbol{\omega}}\| \cdot \Delta t_k = \|\hat{\boldsymbol{\omega}}\| \cdot \frac{250 - k}{1000} \tag{31}$$

Recall that $\boldsymbol{\omega}$ is the axis of rotation and assumed constant over the sub-interval. It is therefore the same in all (instantaneous) subsample coordinate frames.

Centripetal Compensation

An estimate for the kinematic effect that results from having the accelerometer mounted with an offset from the structure's spin-center (i.e. the center-of-mass) is obtained by replacing the values in the dynamical terms with current-best-estimates. In the case of the attitude transforms $\mathcal{A}$ and the angular rate $\boldsymbol{\omega}$, these estimates come directly from the on-board attitude estimate whose accuracy is governed by the star sensor measurements and MEKF solution. The only other estimate needed is the offset of the accelerometer sensor heads from the system's center-of-mass $(\hat{\mathbf{r}}_{cd})$.

$$E\left[\left\{\underset{i\leftarrow b}{\mathcal{A}}[\boldsymbol{\omega}]^\times \mathbf{r}_{cd}\right\}_{t_1}^{t_2}\right] = \underset{i\leftarrow b_2}{\hat{\mathcal{A}}}\,[\hat{\boldsymbol{\omega}}(t_2)]^\times \hat{\mathbf{r}}_{cd}(t_2) - \underset{i\leftarrow b_1}{\hat{\mathcal{A}}}\,[\hat{\boldsymbol{\omega}}(t_1)]^\times \hat{\mathbf{r}}_{cd}(t_1) \tag{32}$$

It is worth emphasizing the efficiency of this result. Since the centripetal correction is applied to the integrated acceleration—and is itself a velocity-correction—it is applicable over any timespan with just this simple two-term computation. Even if the time-interval (t_1, t_2) spans multiple revolutions of the base-body, this correction is exact to within the accuracy of our estimates.

Center-of-Mass Knowledge Knowledge of the location of the center-of-mass of a 939-kg observatory with eight appendages and slightly over 411-kg of hydrazine fuel proved to be one of the most challenging aspects of the mission. The risk to maneuvering accuracy was mitigated by a combination of techniques. First, the mechanical book-keeping on the structure was accomplished to an accuracy impractical prior to the extensive use of solid CAD models of an assembly.[8] Secondly, the calculated mass properties for the fully-stowed (dry) spacecraft were verified prior to launch using a spin-balance facility *Miller table*. Additionally, a number of propellant loading/unloading tests and Monte Carlo simulations were performed to bound the final range of "shapes" the fuel—constrained by an elastomer-diaphragm—might take in the four cylindrical tanks prior to launch. Lastly, a series of on-orbit calibration maneuvers were performed while capturing the 1 kHz accelerometer data. The telemetered data was processed on the ground using an augmented MEKF for parameter estimation/system-identification. Ultimately, it is believed the CM statistical knowledge-accuracy achieved was better than 1-millimeter (1σ) for the observatories prior to Axial Double Probe and Spin-plane Double Probe (SDP) deployment. It can be seen by inspection of Eq. (22) that if elements of the angular rate are constant, a fixed error in center-of-mass knowledge $\boldsymbol{\delta r}_c$ would yield an error $\boldsymbol{\omega}^{\times}\boldsymbol{\omega}^{\times}\mathbf{r}_{cd}$ that is indistinguishable from a sensor bias. A future publication is being prepared that will explore this and the larger topic of MMS system identification in greater depth.

Sensor Head Offsets A subtlety exists with centripetal compensation that is due to the multiple sensor-heads $(n \geq 3)$ that are required for a full vector solution. It is physically impossible for the uni-axial heads to be exactly co-located, so the centripetal compensation must account for each of the small head-offsets. MMS was fortunate that this correction could be applied after integration—to the accumulated velocity-output. In general, when the sensing axes are not all mutually orthogonal, the head-offset correction would need to be applied to the acceleration measurements directly, before they are collapsed in to a single vector-quantity via Eq. (24).

Multi-body Effects

Multi-body effects—more precisely the internal flexure of the deployable appendages and flow of fuel—defeats most attempts at simple analytic approximation in the sense of the classical rotating rigid-body equations. In the course of analyzing MMS, a number of linearized motion models were used to gain insight regarding the system modes,[9] but ultimately it was the non-linear time-domain simulations of the spacecraft that were used to predict the multi-body response of the system. Specifically, the boom-appendage and fuel-slosh dynamics were modeled using multiple rigid bodies connected by rotational joints.[10]

However, regardless of the complexity of the flexible-body dynamic motion, it is true that its effect on the spacecraft is non-propulsive. As a result, the expected value of the center-of-mass motion term in Eq. (28) will—over a sufficiently long interval—integrate to zero. With regards to acceleration feedback correction/compensation, CM-motion during a maneuver was ignored in the MMS estimator-design with the caveat that the nutation and wire-boom deflections were minimized during the maneuver using interleaved angular momentum control-pulses for which the moniker DVDH was coined.

One area in which the boom flexibility appears directly is the MEKF. It was shown analytically and via simulation that the state-propagation is improved if an "effective inertia" is used for the filter's rigid-body approximation of the rotational dynamics. Following the method of Zimbelman and Walker,[11] the effective inertia about the spin-axis I_{eff} used in the MEKF is defined as

$$I_{\mathsf{eff}} \equiv I_{\mathsf{base}} + \left(\frac{r_{\mathsf{sdp}}}{r_{\mathsf{sdp}} + L_{\mathsf{sdp}}} \right) I_{\mathsf{sdp}} \tag{33}$$

where r_{sdp} is the radial distance from the spin-axis to the SDP pivot-point, L_{sdp} is the distance along the wire-boom to the SDP's center-of-mass, and I_{sdp} is the SDP's second mass-moment of inertia about its own center-of-mass as if it were a rigid rod. A similar expression also is used for the effective inertia's about the spacecraft's transverse axes.

Bias Estimation

A dominant factor in the overall maneuver execution error of the system is the integral of the intrinsic electro-mechanical biases. The MMS sensor has the potential for a non-stationary bias on the order of $\pm 2000 \mu g$, with a one-year composite bias repeatability of 105 μg.[12] However, over a much shorter period of twelve hours, the bias stability (in a temperature controlled environment) is less than ± 1 μg. As a result, over the duration of a maneuver ($\leq$ 90 minutes for MMS), the bias is nearly constant and is compensated internally in the AMS by subtracting a per-maneuver bias estimate $\hat{\mathbf{b}}$ from the acceleration measurement subsamples before they are added to the running velocity total. The bias-residual is defined as the error in the bias estimate ($\boldsymbol{\delta b} \equiv \mathbf{b} - \hat{\mathbf{b}}$). The estimate $\hat{\mathbf{b}}$ is itself obtained from an independent filter internal to the AMS. Just like an attitude Kalman filter uses the inertial reference of star sensor measurements to estimate the biases in gyros, the inertial reference of a non-thrusting period of spacecraft orbit ($\Delta \dot{\mathbf{v}}_c = \mathbf{0}$) is sufficient to determine the intrinsic bias of the accelerometers. In the case of MMS, a 6^{th}-order, cascaded (bi-quad) low-pass filter was used with a frequency break-point set at 0.004 Hz (4.2 minutes). Due to its long time-constant, the bias-residual filter requires 30-minutes of quiescent data prior to each maneuver in order to settle to within ± 1 μg of its steady-state solution. In order to speed-up convergence and also compensate for any base-body nutation, the expected value (or mean) of the gyro-dynamic bias is subtracted from the bias-residual filter's input. The mean gyro-dynamic bias is determined by taking the expected value of Eq. (25) and expanding for $\mathbf{a}_d$ using Eq. (22).

$$E\left[\mathbf{a}_k\right] = E\left[\dot{\boldsymbol{\omega}}^{\times}\right] \mathbf{r}_{cd} + E\left[\boldsymbol{\omega}^{\times}\boldsymbol{\omega}^{\times}\right] \mathbf{r}_{cd} - E\left[2 \cdot \boldsymbol{\omega}^{\times}\dot{\mathbf{r}}_c + \ddot{\mathbf{r}}_c\right] + E\left[\mathbf{b}\right] + E\left[\boldsymbol{\eta}\right] \tag{34}$$

Recognizing that the expected value of the zero-mean noise and multi-body (internal flexure) terms are both necessarily zero, $E\left[\mathbf{b}\right]$ is the bias estimate $\hat{\mathbf{b}}$ being sought, and add to that $E\left[\mathbf{a}_k\right]$ is approximately the low-pass bias-residual filter's output, to obtain the following new expression

$$\hat{\mathbf{b}} = \underbrace{E\left[\mathbf{a}_k\right]}_{\text{bias filter output}} - \underset{b\leftarrow p}{\mathcal{A}} \left(E\left[\dot{\boldsymbol{\omega}}_p^{\times}\right] \underset{p\leftarrow b}{\mathcal{A}} \mathbf{r}_{cd} + E\left[\boldsymbol{\omega}_p^{\times}\boldsymbol{\omega}_p^{\times}\right] \underset{p\leftarrow b}{\mathcal{A}} \mathbf{r}_{cd} \right) \tag{35}$$

where $\boldsymbol{\omega}_p$ is the angular rate with respect to inertial of a body-fixed frame p aligned with the spacecraft's principal axes. The principal-axis frame was introduced here because, for an axisymmetric major axis spinner, there is a well known analytic solution for its motion[13]

$$\omega_1(t) = w_1(0)\cos\lambda t - \omega_2(0)\sin\lambda t \tag{36}$$

$$\omega_2(t) = w_1(0)\sin\lambda t + \omega_2(0)\cos\lambda t \tag{37}$$

$$\omega_3(t) = \omega_3(0) \tag{38}$$

where λ is the nutation frequency derived from the principal moments of inertia ($I_3 > I_2 > I_1$) and (constant) major-axis spin-rate as follows

$$\lambda = \frac{I_t - I_3}{I_t}\omega_3 \tag{39}$$

where the transverse moment of inertia $I_t \equiv I_1 = I_2$ in an axisymmetric body (or can be approximated using the geometric mean $I_t \approx \sqrt{I_1 \cdot I_2}$ in the nearly axisymmetric case). From the coupled motion equations, it can be determined by inspection that $E\left[\dot{\boldsymbol{\omega}}_p\right] = \mathbf{0}$ and

$$E\left[\boldsymbol{\omega_p}^{\times}\boldsymbol{\omega_p}^{\times}\right] \underset{p\leftarrow b}{\mathcal{A}}\mathbf{r}_{cd} = \begin{bmatrix} -w_s^2 \cdot r_1 + E\left[\omega_1\omega_2\right] r_2 - E\left[\omega_2^2\right] r_1 \\ -w_s^2 \cdot r_2 - E\left[\omega_1^2\right] r_2 - E\left[\omega_1\omega_2\right] r_1 \\ -\left(E\left[\omega_2^2\right] + E\left[\omega_1^2\right]\right) r_3 \end{bmatrix} \tag{40}$$

$$= \underbrace{\begin{bmatrix} -w_s^2 \cdot r_1 \\ -w_s^2 \cdot r_2 \\ 0 \end{bmatrix}}_{\text{spin bias}} + \underbrace{\begin{bmatrix} -\frac{1}{2}\omega_t^2 \cdot r_1 \\ -\frac{1}{2}\omega_t^2 \cdot r_2 \\ -\omega_t^2 \cdot r_3 \end{bmatrix}}_{\text{nutation bias}} \tag{41}$$

where $\omega_s \equiv \omega_3(0)$ and $\omega_t \equiv \sqrt{w_1^2 + w_2^2}$ are the magnitude of the spin and transverse rates in the principal axis frame respectively. The first term in Eq. (41) for MMS has a magnitude of 3950 μg, however the nutation term is small—on the order of a few micro-g—and to the best of our knowledge, had not been specifically identified in the published inertial-navigation literature.

As an additional consideration, signal-aliasing of the wide-band noise must be carefully managed to prevent corruption of the final bias estimate. For this reason, the bias residual filter was located inside the AMS, leveraging its ability to process the high-frequency data directly.

Principal Axis Alignment Since the average instantaneous spin of the spacecraft is about the major principal axis, the orientation of the principal-axes frame with respect to the body-fixed axes is estimated prior to each maneuver using a low-pass filter. This estimator resides in the ACS flight-software and operates on the body's rate-estimate $\hat{\boldsymbol{\omega}}$ produced by the attitude determination MEKF at 4 Hz. Recalling *Poinsot's construction*[5,13] for an axisymmetric body, the body-cone angle β can be determined from the components of the filtered angular rate $\boldsymbol{\omega}_f$ as

$$\beta = \tan^{-1}\left(\frac{\sqrt{\omega_{f_x}^2 + \omega_{f_y}^2}}{\omega_{f_z}}\right) \tag{42}$$

This angle is the second rotation in a classic 3-1-3 ($\phi - \beta - \psi$) *Euler angle sequence* that transforms from the body to the principal axes frame. The first rotation in the sequence, ϕ, is

$$\phi = \tan^{-1}\left(\frac{\omega_{f_y}}{\omega_{f_x}}\right) + \frac{\pi}{2} \tag{43}$$

and the final clocking angle ψ of the minor and intermediate axes about the major axis may be chosen arbitrarily, since it does not affect the bias estimation calculation in Eq. (41) (nor do the exact magnitudes of the principal moments). The final set of rotations can then be used to construct the direction cosine matrix $\underset{p\leftarrow b}{\mathcal{A}}$ or equivalent quaternion.

Effects of Bias Integration in a Rotating Frame An important consideration for maneuver knowledge error is what happens on a spinning platform to a bias that is constant in the body-frame after it is transformed to the inertial-frame and integrated. For a pure z-axis rotation, we have

$$\mathbf{v} = \int_t^{t+\Delta t} \underset{i\leftarrow b}{\mathcal{A}}(\tau) \cdot \mathbf{b} \cdot d\tau = \int_t^{t+\Delta t} \begin{bmatrix} \cos\omega_z\tau & \sin\omega_z\tau & 0 \\ -\sin\omega_z\tau & \cos\omega_z\tau & 0 \\ 0 & 0 & 1 \end{bmatrix} \begin{bmatrix} b_x \\ b_y \\ b_z \end{bmatrix} d\tau \tag{44}$$

$$= \begin{bmatrix} \frac{b_x}{\omega_z}\sin\omega_z\Delta t + \frac{b_y}{\omega_z}(1-\cos\omega_z\Delta t) \\ \frac{b_x}{\omega_z}(\cos\omega_z\Delta t - 1) - \frac{b_y}{\omega_z}\sin\omega_z\Delta t \\ b_z\Delta t \end{bmatrix} \tag{45}$$

This simple result shows that the effect of integrating bias residuals along the two transverse axes is both cyclical and bounded. However, the axial $\Delta\mathbf{v}$ knowledge error due to integrated bias estimation error grows linearly with time. In contrast, the RMS of noise-driven velocity random walk (discussed next) only increases as the $\sqrt{\Delta t}$. For all practical MMS maneuver durations, the integrated axial bias residual is the dominant source of error. This qualitative difference due to direction (axial/radial) is revealed in Figure 3 during a portion of a high-fidelity simulation of the fully-deployed spacecraft executing a 5 m/sec maneuver.

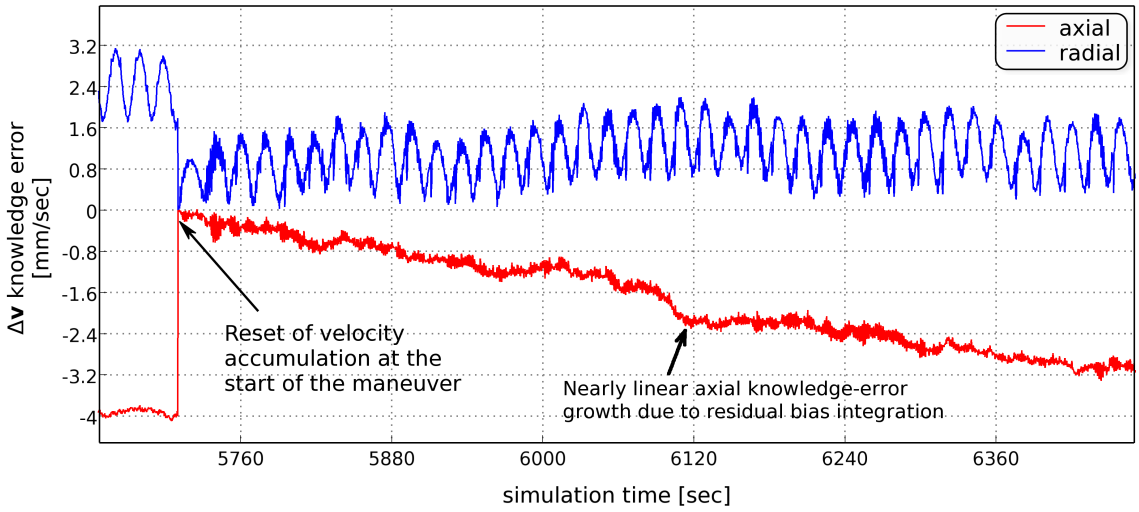

Figure 3. Simulation of Axial and Radial Knowledge Errors

In order for MMS to meet its mission requirements, it was expected that the composite bias-residual/CM-knowledge-bias error would be $\leq 1\,\mu g\ (1\sigma)$ prior to a maneuver.

Velocity Random Walk

The final right-hand term in Eq. (28) is the result of conceptually integrating the wide-band stationary noise of the accelerometer. This error source is assumed to be driven by an unspecified electrical-thermal source. An estimate of its effect on velocity can be determined by taking it expected value

$$E[\boldsymbol{\Delta v}_\eta] = E\left[\int_{t_1}^{t_2} \underset{i\leftarrow b}{\mathcal{A}} \cdot \boldsymbol{\eta}\, d\tau\right] \approx \int_{t_1}^{t_2} E\left[\boldsymbol{\eta}\right] \cdot d\tau = 0 \tag{46}$$

where the body to inertial transformation $\mathcal{A}$ may be dropped because the noise is temporally uncorrelated. While the expected value of the noise is zero-mean—and will not bias the estimate of the velocity—the variance (mean-squared value) of the integrated noise is

$$E[\boldsymbol{\Delta v}_\eta^2] \approx \int_{t_1}^{t_2} E\left[\boldsymbol{\eta}^2\right]\, d\tau = \int_{t_1}^{t_2} \frac{1}{2\pi} \int_{-\infty}^{\infty} S(j\omega)\, d\omega \cdot d\tau \tag{47}$$

where $S(j\omega)$ is the power spectral density (PSD) of the noise, and ω is a frequency in rad/s—not to be confused with the base-body angular rate $\boldsymbol{\omega}$. If the input is assumed to be *band-limited white noise*, then the PSD is a constant $A/2$ within the pass-band (f_{hz}), and zero otherwise. The velocity variance becomes

$$E[\boldsymbol{\Delta v}_\eta^2] = \int_0^{\Delta t} E\left[\boldsymbol{\eta}^2\right]\, d\tau = \int_0^{\Delta t} \frac{1}{2\pi} \int_{-2\pi f_{\text{hz}}}^{2\pi f_{\text{hz}}} \frac{A}{2}\, d\omega \cdot d\tau = \int_0^{\Delta t} A\, f_{\text{hz}}\, d\tau = A\, f_{\text{hz}}\, \Delta t \tag{48}$$

The QA3000 specification asserts the root-mean-squared noise ($a_{\text{rms}} = \sqrt{E[\boldsymbol{\Delta v}_\eta^2]}$) should be less than 8 μg_{rms} in the frequency range 0-10 Hz, and 80 μg_{rms} from 10-500 Hz. This implies that if a (single-sided) periodogram of acceleration-samples over a large time-interval was computed, its expected magnitude (A) over a given frequency range (e.g. Δf_{hz} = 10 Hz) should be less than

$$A_{0-10\,\text{hz}} \leq \frac{(a_{\text{rms}})^2}{\Delta f_{\text{hz}}} = \frac{8^2\, \mu g^2}{10\,\text{Hz}} = 6.4\, \frac{\mu g^2}{\text{Hz}} = 615.9 \frac{\left(\frac{\mu\text{m}}{\text{s}^2}\right)^2}{\text{Hz}} \tag{49}$$

Figure 4 shows this is indeed the case for a sample taken from an non-maneuvering MMS-1. With

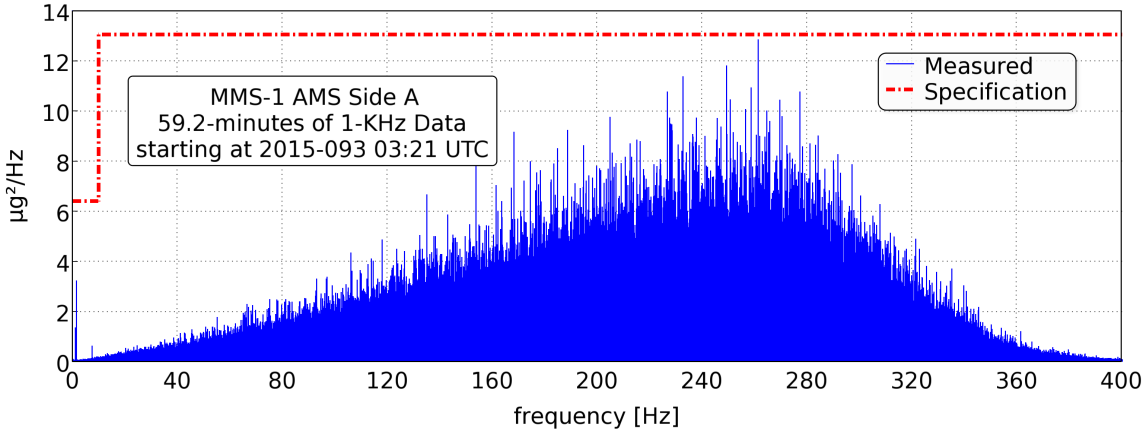

Figure 4. PSD of MMS-1 AMS 1 kHz Acceleration Data

this base-band noise input driving an integrator-plant, the velocity random walk is then

$$(\boldsymbol{\Delta v}_\eta)_{\text{rms}} \leq \sqrt{A_{0-10\,\text{hz}} \cdot \Delta t} = \left(24.8\, \frac{\mu\text{m}}{\text{s}} \cdot \sqrt{\text{Hz}}\right) \cdot \sqrt{\Delta t} \tag{50}$$

It can be shown that the noise-response is dominated by the content in the base-band (0-10 Hz) due to low-pass nature of the integrator (-20 dB/decade). This mitigation strategy for this error-source is to limit size of the velocity-accumulation window tightly on the thrusting portion of a maneuver.

Other Error Sources

Non-Linearity At operational temperatures, the non-linearity error (of the scale-factor) over the QA3000's dynamic range was calculated to be less than 150 ppm.

Thermal Effects. Nearly all elements of the AMS exhibit some degree of temperature dependence that could affect performance. For MMS, these error were minimized by actively controlling the thermal environment—limiting variations during maneuvers to with ± 1-degree Celsius. Additionally, a number of temperature corrections are applied internally to the acceleration samples by the AMS based its own internal thermistors with 0.1° resolution.

Scale Factor Through careful component selection, and by performing extensive ground calibration of the AMS in an isolated environment (NASA Glenn Research Center, Plum Brook Facility), ZIN was able to limit expected scaling factor errors to less than 872 ppm.

Non-Orthogonality / Sensor Alignment Alignment of the individual sensor-head axes was controlled by machine tolerances, thermal compensation during flight, and verified by ground metrology within an accuracy of 115-arcsec per axis. This error—contributing less than 0.2-ppm of scale-factor error and mapping directly to directional error ($115\sqrt{3}$ arcsec = 0.055°)—does not dominate.

Quantization The resolution of the sensor is better than $0.8\mu g$. As a result, quantization through discretization is not considered a significant source of error.

Frequency Response / Structural Dynamics The AMS is mounted on a shock/vibration isolation system designed by MOOG/CSA Engineering. Nevertheless, the structural response seen at the accelerometers due to thruster firings is very pronounced—at times, greater than 75% of saturation. The MMS structure exhibits a number of modes in the 30-300 Hz range that pollute the AMS acceleration output. Fortunately, due the low-pass characteristics of integration, the ripple-effect on maneuver velocity knowledge is below 1 mm/sec (see Figure 5), and the small error can be absorbed in the performance budget. Furthermore, the structural-response damps quickly—only three-seconds of padding is required at the end of each maneuver to account for ring-down.

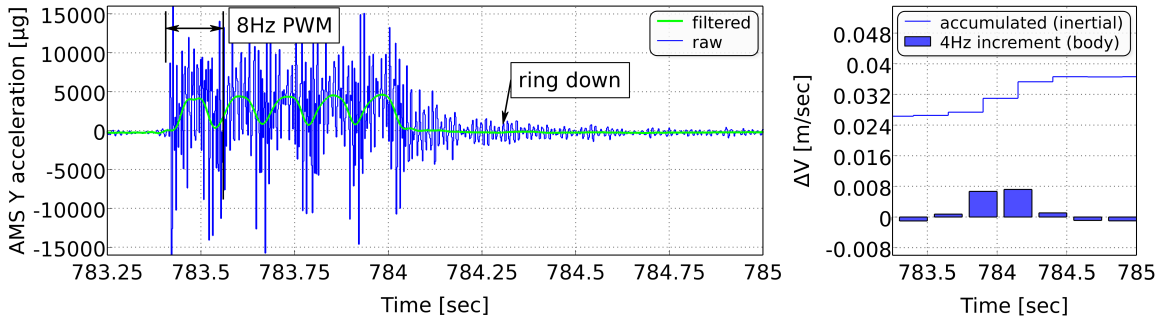

Figure 5. Structural Modes Effect on Accumulated Velocity (telemetry)

Summary of Velocity Estimation Method

Having first briefly explained how the spacecraft constructs its attitude and rate knowledge from star sensor measurements, details were then provided on an acceleration measurement model. It was shown that directly integrating the acceleration-samples would not produce an accurate estimate of the spacecraft's center-of-mass velocity change, so the necessary corrections were derived in detail. All of the compensations explained may be categorized as follows:

- **bias estimation** *(pre-maneuver)*—The ACS and AMS use the angular rate with long duration low-pass filters to arrive at an accurate intrinsic sensor-head bias estimate.
- **bias and sculling correction**—The AMS uses the bias and angular rate estimates to correct and sum the (1 kHz) acceleration-samples in order to produce a (4 Hz) incremental velocity.

- **centripetal correction and inertial summation**–The angular rate is used to apply centripetal correction to the (4 Hz) incremental velocity output, and the total inertial (ECI J2000) velocity-change imparted to the spacecraft is accumulated.

ATTITUDE, ANGULAR MOMENTUM, AND TRANSLATIONAL CONTROL

Actuators (thrusters)

Both attitude and orbital control of the observatories are accomplished using twelve hydrazine mono-propellant thrusters—four AMPAC 1-lbf (4.4 N) thrusters are directed axially ($\pm$z) and eight Aerojet 4-lbf (17.8 N) thrusters radially ($\pm$y). The minimum impulse bit for the Aerojet designed thrusters ranges throughout the mission from 0.13–0.26 N-m-sec, which corresponds to a 20 millisecond pulse. In addition to a continuous firing mode, the engine-value-driver is capable of modulating the duty-cycle of the output on 8 Hz boundaries. This pulse-width-modulation allows for balancing of torques during translational maneuvers that minimizes attitude perturbations.

Velocity Control Vector Definitions

With the definition for the truth-states of Eq. (28) in-hand, a number of other important control-vector quantities may also be derived. First, the imparted velocity estimate $\Delta\hat{\mathbf{v}}_c$ is defined as the expected value of the true velocity-change,

$$\Delta\hat{\mathbf{v}}_c(t_1, t_2) = E\left[\Delta\mathbf{v}_c(t_1, t_2)\right] \tag{51}$$

The maneuver knowledge-error ($\delta\tilde{\mathbf{v}}$) is the difference between the estimate and truth

$$\delta\hat{\mathbf{v}}(t_1, t_2) = \Delta\hat{\mathbf{v}}_c(t_1, t_2) - \Delta\mathbf{v}_c(t_1, t_2) \tag{52}$$

The true performance metric for the system is the control-error $\delta\mathbf{v}$, which is the difference between the commanded velocity-change (target) and the truth

$$\delta\mathbf{v}(t_1, t_2) = \Delta\mathbf{v}_c(t_1, t_2) - \Delta\mathbf{v}_{\mathsf{tgt}}(t_1, t_2) \tag{53}$$

Finally, the definition of the servo-error ($\delta\mathbf{v}_{\mathsf{servo}}$) is the difference between the target and estimate,

$$\delta\mathbf{v}_{\mathsf{servo}} = \Delta\mathbf{v}_{\mathsf{tgt}}(t_1, t_2) - \Delta\hat{\mathbf{v}}_c(t_1, t_2) \tag{54}$$

and is the quantity that the controller actively regulates.

Velocity Control

The ΔV controller follows the design principals of a classic tracker—with both a time-varying target, and velocity-estimate feedback. A predetermined velocity-change profile is uploaded to the spacecraft prior to each maneuver. The trajectory is in the form of a piece-wise linear look-up table—ΔV in ECI J2000 versus spacecraft time. There are very few constraints on the nature of the profile. For example, it may be non-monotonically increasing in magnitude, and/or it may possess arbitrary spacial curvature. However, it must be constructed with a care towards the saturation limits of the thrusters or the system will perpetually lag behind the target—potentially failing to regulate the servo-error sufficiently within a given maneuver window. The controller is entirely responsible for the mapping of velocity-commands—specified in the inertial frame—to the appropriate grouping of thrusters (i.e. "bank") capable of delivering an ideally torque-less translational force to the spacecraft. The projection of the servo-error into cylindrical coordinates determines if an axial or radial bank is a proper candidate for actuation.

Axial Thrusting On a spinning spacecraft, axially-aligned thrust is conceptually simpler. Since the spacecraft's center-of-mass radial offset from the spin-axis is nominally zero, no torque-balancing via pulse-modulation is attempted. However, since the axial thrust is always well-aligned with the axial projection of servo-error, in order to reduce the amount of valve-cycling and chattering between the top and bottom ($\pm$z) banks, the controller is designed to utilize a dead-band, and limits commanding to roughly once every quarter spin period. Since translational and rotational control is interleaved (and translational-control is given priority), this "packeting" of axial-actuation also offers a potential benefit by freeing those thrusters for full momentum/attitude-control. The qualifier "full" was applied to the previous statement because axial off-pulsing of a single thruster in a pair is also sometimes necessary—especially when a ΔV profile contains a dominant axial-component and/or the (diaphragm-constrained) fuel-mass is unbalanced about the spin-axis.

Radial Thrusting The MMS radial thrusters are arranged in two banks of four, each directed along the positive and negative y-axis respectively. Pulse-Width-Modulation (on 8 Hz boundaries) of the upper or lower pairs in each quad facilitates torque-balancing. This arrangement offers two opportunities per spin for thrust along a given inertially-fixed direction (roughly every 10-seconds). In order to avoid inducing directional error, the radial actuation is centered around the servo-error's projection in the spin-plane. Because the controller tracks a time-varying velocity-profile, the burn-centering problem is non-trivial. The precise timing affects the burn-vector and vice versa—therefore an iteration solver is employed to resolve target-centering down to a millisecond resolution. Explicitly, for a given servo-error, the current rate estimate can be used to predict the time at which the thrusters will align with the center of the required burn-arc. However, at the predicted center-time, the target will have most likely shifted—resulting in a slightly different servo-error projection, *ad infinitum*. Fortunately, convergence is typically achieved within a few iterations. Also, to prevent the controller from constantly lagging it's target, a quarter spin-period "look-ahead" strategy is employed. As shown in Figure 6 this 5-seconds of time-bias keeps the servo-error straddling the velocity-profile, and speeds up entry into a fine-tuning "trim" phase at the end of each maneuver. Similar the axial control strategy, dead-bands are employed to reduce the wasting of fuel due to chatter.

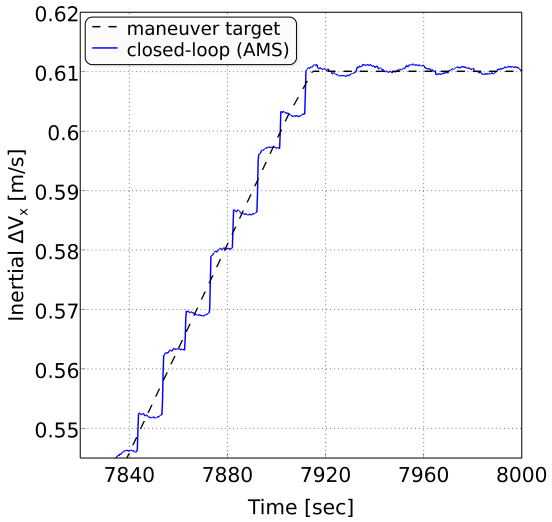

Figure 6. Velocity Controller Telemetry (FI-116)

Momentum Control The spin-axis inertial pointing direction is important to the MMS science instrument suite. For this reason, each observatory performs a momentum-adjustment (ΔH) immediately following every ΔV. While the specifics of the ΔH control-logic are not examined here (see the reference[14]), it is also important to hold pointing, minimize nutation, and maintain spin during a ΔV-maneuver—not only for the instruments, but also for accurate velocity-estimation. Momentum control during a ΔV maneuver (DVDH) employs the same Lyapunov-based controller as the stand-alone ΔH mode, with two main differences—the aforementioned off-pulsing of axial-thrusters, and the frequency of the control (e.g. while DVDH is only allowed to actuate up to once every 3-seconds in order to avoid structural resonance with the two ADP booms, ΔH-mode is typically slower).

SYSTEM ROBUSTNESS

Two major concerns of control system design are robustness in stability and performance in the presence of plant uncertainty. For MMS, exhaustive Monte Carlo simulations were used to address these twin concerns. Following the statistical methodology of Hanson and Beard,[15] 99% confidence criteria (1% consumer risk) was selected that requires zero failures over a sample-size of 3410 runs.

This criteria was tested repeatedly using GSFC's Freespace Simulation Environment[16] to statistically vary over 250 model parameters—resulting in hundreds of thousands of time-domain simulations of maneuvers at full model-fidelity. Figure 7 depicts one example of these results, and is annotated with the performance criteria used to determine execution error acceptance for a formation-maintenance class of closed-loop maneuver (0-10 m/sec). The scatter plots of maneuver magnitude and directional error from 3500 runs shows ample margin versus the 3σ closed-loop (AMS) requirement (in cyan).

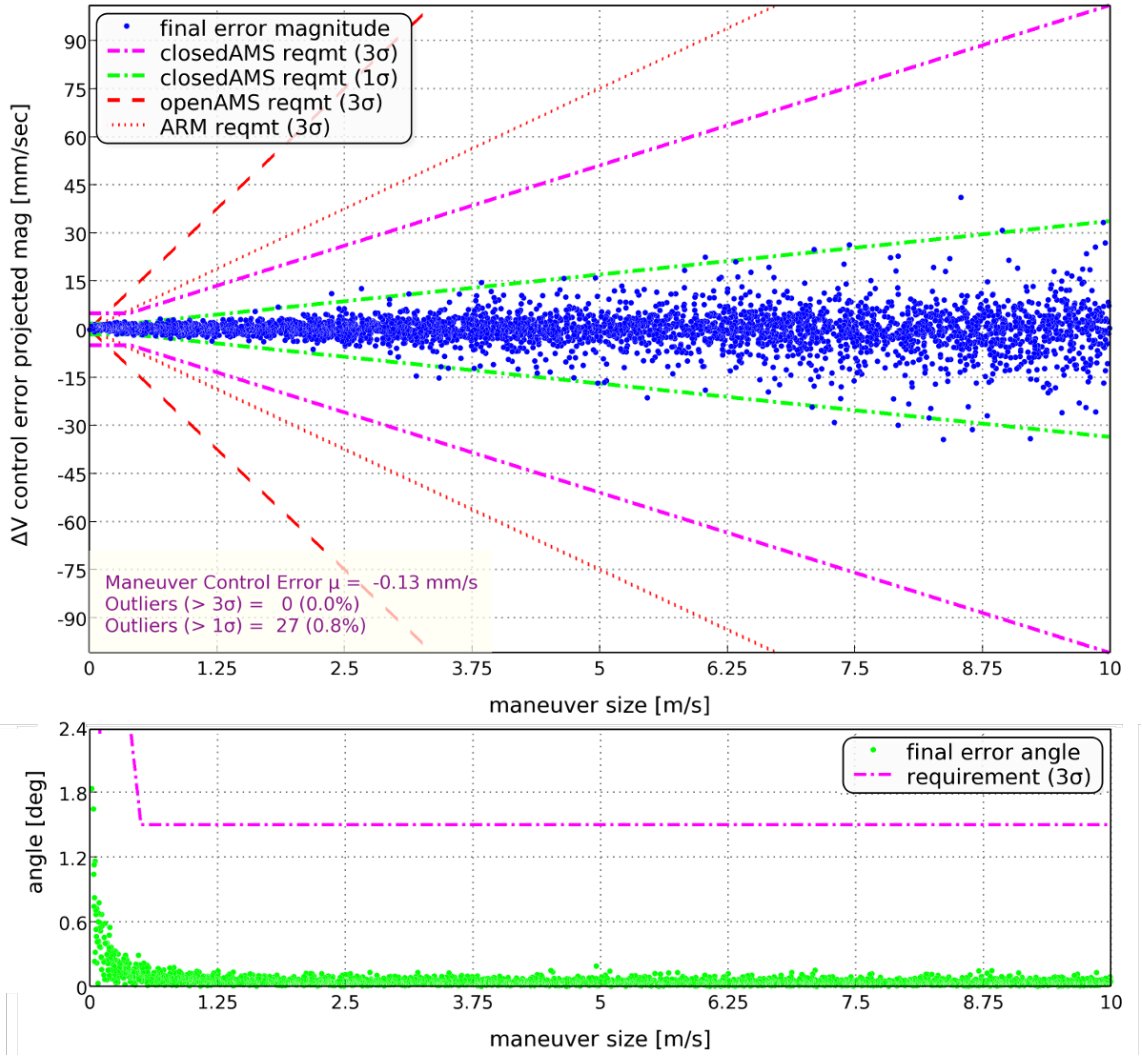

Figure 7. Monte Carlo Results for Formation Maintenance Maneuvers

MMS MISSION PERFORMANCE

Open-loop Maneuver

During early observatory commissioning, a series of perigee-raising maneuvers were performed to lift the orbits above the launch vehicle insertion-altitude and reduce atmospheric drag. Because these maneuvers were relatively large, and occurred before the AMS performance had been fully verified, they were executed open-loop (i.e. without accelerometer feedback). Although it was not in the control-loop, the AMS was still available to monitor the performance of the open-loop controller. The data shows that, despite a qualification test-program that attempted to characterize thruster-performance prior to launch, the propellant-system still exceeded its expected-value by approximately 8% for the radials (nominally 4-lbf). This only underlies how difficult it is to predict total system behavior during mission development, and emphasizes the need for closed-loop control when a high degree of accuracy is required. One example of a difficult problem to characterize is performance during warm-up of the hydrazine catalyst-beds. Flight and ground-test data showed that, during the first 20-seconds after a cold-start, thrust could start as much as 15% lower than the final steady-state output. The plot of flight-telemetry shown in Figure 8 emphasizes the divergence between the open and closed-loop $\Delta \mathbf{v}_c$ estimates for an MMS-1 perigee-raise maneuver.

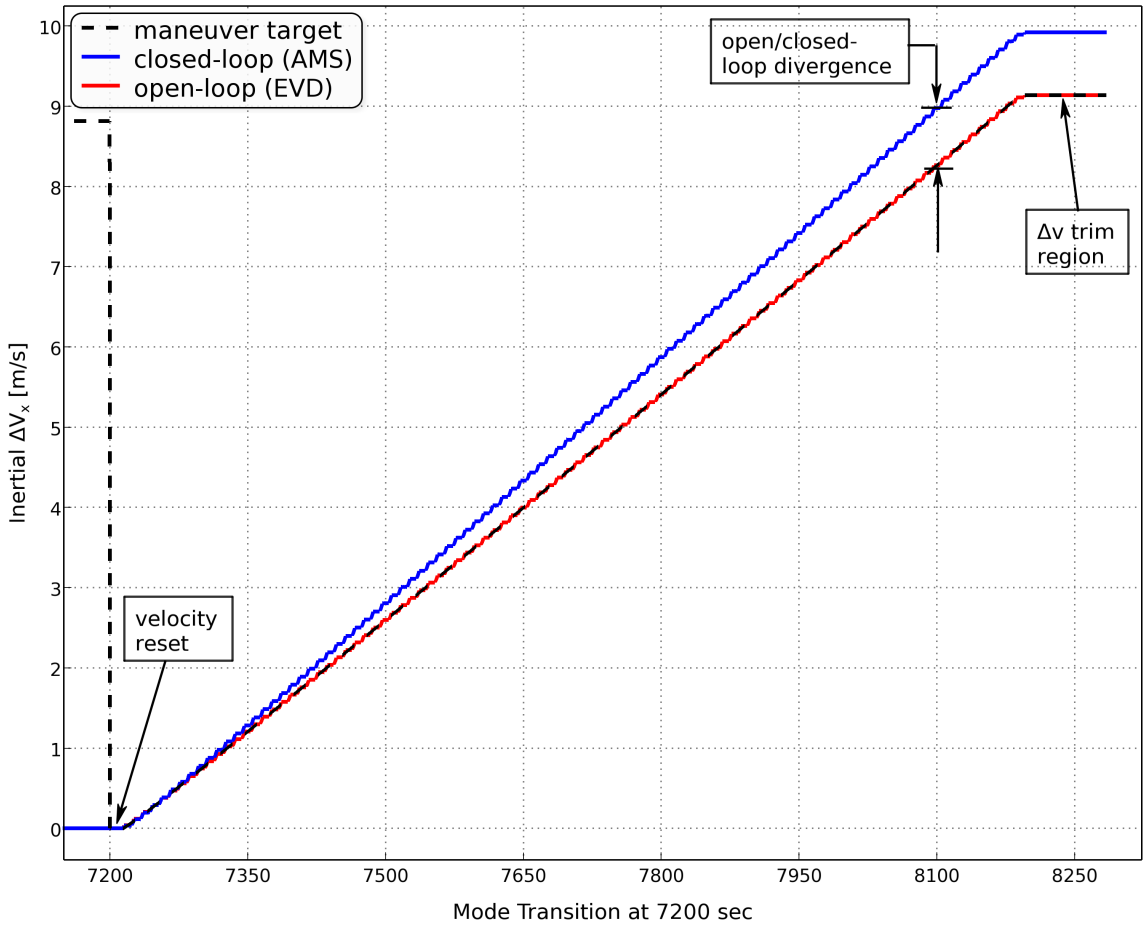

Figure 8. MMS-1 Open-loop Maneuver Performance Comparison to Closed-loop Estimate

Closed-loop Maneuvers

The best avenue for determining the true closed-loop performance is through post-maneuver orbit determination. The GSFC developed NAVIGATOR[17] Global Positioning System (GPS) and GPS-Enhanced Onboard Navigation System (GEONS) units are collectively providing autonomous orbit determination with a record-breaking 5 meters (3σ) semi-major axis (SMA) accuracy.[18] After the first few closed-loop formation initialization maneuvers for MMS commissioning, the following performance has been verified

Maneuver (DOY)	Obs ID	Final Target Magnitude mm/s	GEONS Solution Semi-major Axis Δ-error	Final Servo-Error mm/s	Final Servo-Error % target	AMS Bias Estimate (μg) X	AMS Bias Estimate (μg) Y	AMS Bias Estimate (μg) Z
GS-095 (163)	1	118.6	-1.14%	1.5	1.25%	114.7	78.9	49.6
	2	18.3	-0.57%	1.0	5.73%	94.3	93.9	47.3
	3	46.9	-0.73%	1.1	2.27%	75.2	92.5	140.1
	4	77.0	0.55%	1.1	1.44%	108.3	96.1	125.1
FI-116 (184)	1	0	—	—	—	115.3	77.4	49.7
	2	4077.5	-0.79%	1.0	0.03%	95.0	94.0	47.5
	3	9175.6	-0.26%	0.2	0.00%	76.9	94.3	140.9
	4	4452.1	-0.26%	1.2	0.03%	107.2	93.9	125.4
FI-118 (190)	1	0	—	—	—	—	—	—
	2	3511.6	-0.61%	0.8	0.02%	93.7	94.0	47.6
	3	4149.7	-0.18%	1.3	0.03%	76.9	94.7	140.8
	4	6068.7	-0.27%	1.3	0.02%	106.9	95.5	125.3

While the error in targeted semi-major axis does not equate with controller-error ($\delta\mathbf{v}$), SMA is directly linked to the orbital speed (e.g. the *vis-viva* equation). These early results indicate that the fleet is maneuvering successfully within the 3σ total mission requirements that are an amalgamation of ACS execution and flight-dynamics planning errors. These results are particularly encouraging considering the sizes of the GS maneuvers, since high percent-accuracy is more challenging for small maneuvers. The sample mean $\bar{\mu}$ of these maneuvers is -0.068%, with a sample standard deviation $\bar{\sigma}$ of 0.637%. Based on this relatively small sample size of 10 cases, we can state with a 90% confidence that the true standard deviation lies in the range of 0.465–1.048%, with the caveat that the distribution of maneuver errors is assumed Gaussian. Ultimately, the criteria for a successful MMS maneuvering-system design will be the length of time for which a high-quality formation can be preserved—which will be measured in the frequency of corrective maneuvers. This will be especially evident when the formation moves from its current average separation of approximately 160 km down to as little as 4 km.

ACKNOWLEDGMENTS

We sincerely appreciate the efforts of Julie Thienel, Juan Raymond, Joseph Sedlak, Russell Carpenter, John Van Eepoel, Ken London, Scott Tucker, Conrad Schiff, and F. Landis Markley for numerous discussions during model development. ZIN Technologies went above and beyond expectations on the error analysis and testing of the AMS; their team leads included Alan Chmiel, James Bontempo, Gilead Kutnick and Melissa LaBarbera. Finally, we also need to thank the rest of MMS ACS Team: Wendy Morgenstern, Kathie Blackman, Shaun Oborn, Oscar Hsu, Joel Gambino, Suyog Benegalrao, Lia Sacks, Blair Carter, Charles Campbell, Ron Miller, Milton Davis, Stephen Mariconti, John Carro, Micheal Yang, Peter Kutt and Josephine San for getting MMS to flight and making this work.

REFERENCES

[1] C. Gramling, "Overview of the Magnetospheric Multiscale Formation Flying Mission," *Proceeding of the 2009 AAS/AIAA Astrodynamics Specialist Conference*, Pittsburg, PA, October 2015. AAS 09-328.

[2] A. Long, "Navigation Operations for the Magnetospheric Multiscale Mission," *Proceeding of the 25th International Symposium of Space Flight Dynamics*, Munich, Germany, October 2015.

[3] J. K. Thienel, F. L. Markley, and R. R. Harman, "Extended Kalman Filter for MMS State Estimation," *Advances in Astronautical Science*, AAS/AIAA Space Flight Mechanics Meeting, 2009, pp. 1513–1526. AAS 09-202.

[4] F. Markley, "Attitude Error Representations for Kalman Filtering," *Journal of Guidance, Control, and Dynamics*, Vol. 26, No. 2, 2003, pp. 311–317.

[5] F. Markley and J. L. Crassidis, *Fundamentals of Spacecraft Attitude Determination and Control*. Space Technology Library, Springer, 1st ed., 2014.

[6] K. M. Roscoe, "Equivalency Between Strapdown Inertial Navigation Coning and Sculling Integrals/Algorithms," *Journal of Guidance, Control, and Dynamics*, Vol. 24, No. 2, 2001, pp. 201–205.

[7] P. G. Savage, "Strapdown Inertial Navigation Integration Algorithm Design Part 2: Velocity and Position Algorithms," *Journal of Guidance, Control, and Dynamics*, Vol. 21, No. 2, 1998, pp. 208–221.

[8] S. Mariconti, "MMS Mass Properties Report," Tech. Rep. 461-MECH-RPT-0086, NASA/Goddard Space Flight Center, Greenbelt, MD, March 2015.

[9] S. Lai and K. Bhavnani, "Dynamics of Satellite Wire Boom Systems," Tech. Rep. AFCRL-TR-75-0220, Air Force Cambridge Research Laboratories, Torrance, CA, February 1975.

[10] S. Queen, K. London, and M. Gonzalez, "Momentum-Based Dynamics for Spacecraft with Chained Revolute Appendages," *Flight Mechanics Symposium*, NASA Goddard Space Flight Center, Greenbelt, MD, Oct 2005.

[11] D. Zimbelman and M. Walker, "FAST AURORAL SNAPSHOT Performance Using a Multi-Body Dynamic Simulation," *Advances in Astronautical Science*, AAS Spaceflight Dynamics, 1993. AAS 93-334.

[12] M. LaBarbera and J. Bontempo, "MMS Acceleration Measurement System Performance Analysis Summary Report," Tech. Rep. MMSAMS-ANA-003-B, Zin Technologies, Inc., Middleburg Heights, OH, October 2012.

[13] W. T. Thomson, *Introduction to Space Dynamics*. J. Wiley and Sons Inc., 1st ed., 1963.

[14] S. Queen, N. Shah, S. Benegalroa, and K. Blackman, "Generalized Momentum Control of the Spin-Stabilized Magnetospheric Multiscale Formation," *AAS/AIAA Astrodynamics Specialist Conference*, Vail, CO, August 2015. AAS 15-816.

[15] J. M. Hanson and B. B. Beard, "Applying Monte Carlo Simulation to Launch Vehicle Design and Requirements Verification," *AIAA Guidance, Navigation and Control Conference*, Ontario, Canada, August 2010. AIAA 2010-8433.

[16] P. M. Hughes, "NASA Goddard Space Flight Center FY 2006 Internal Research and Development Program," Tech. Rep. 2006-AR-V6, NASA/Goddard Space Flight Center, Greenbelt, MD, 2007.

[17] W. Bamford, J. Mitchell, M. Southward, P. Baldwin, L. Winternitz, G. Heckler, R. Kurishh, and S. Sirotzky, "GPS Navigation for the Magnetospheric Multi-Scale Mission," *Proceedings of the 22nd International Technical Meeting of The Satellite Division of the Institute of Navigation (ION GNSS 2009)*, Savannah, GA, Sept 2009. pp. 1447-1457.

[18] M. Farahmand, "Magnetospheric Multiscale Mission Navigation Performance Using the Goddard Enhanced Onboard Navigation System," *Proceeding of the 25th International Symposium of Space Flight Dynamics*, Munich, Germany, October 2015.